

HI-WPP Mountain Wave Case on a Reduced Radius Sphere

Joe Klemp, Bill Skamarock, and Sang-Hun Park, NCAR

30 May 2014

For the HI-WPP idealized mountain wave test cases on a reduced radius sphere, we have agreed to focus on three model configurations that are variations from the original DCMIP (Ullrich et al. 2012, DCMIP) experiments. These cases are: M1; flow over a quasi two-dimensional ridge that can be compared to published results for uniform flow over a two-dimensional ridge (Schär et al. 2002, SLFLG; Klemp et al. 2003, KSF), M2; flow over a circular mountain that can be compared to 3-D linear analytic solutions for uniform flow over the circular mountain in a Cartesian geometry, and M3; flow with vertical wind shear over a circular mountain as defined in DCMIP test case 2.2 .

Mean atmospheric sounding

The intent for these testcases is to simulate the flow of an atmosphere having constant wind and stability over a specified terrain profile on a reduced radius sphere in the absence of rotation ($\Omega = 0$). Following DCMIP case 2, we initialize the atmosphere with an isothermal mean state at the equator [$T_i(\lambda, 0, z) = T_{eq} = 300$ K] and a zonal wind in solid body rotation with a vertical wind shear (for case M3) specified at the surface such that:

$$u_i(\lambda, \phi, z) \rightarrow u_{eq}(1 + cz) \cos \phi \quad \text{as } z \rightarrow 0, \quad (1)$$

where $u_{eq} = 20 \text{ ms}^{-1}$ and the subscript i refers to the initial undisturbed state. The desired balances in the initial state derive from balancing the gradient wind equation:

$$\frac{\partial \ln p_i}{\partial \phi} = -\frac{u_i^2}{RT_i(\phi)} \tan \phi, \quad (2)$$

together with the hydrostatic equation:

$$\frac{\partial \ln p_i}{\partial z} = -\frac{g}{RT_i(\phi)}. \quad (3)$$

Cross-differentiating (2) and (3):

$$\frac{\partial}{\partial z} \left(\frac{\partial \ln p_i}{\partial \phi} \right) = \frac{g}{RT_i} \frac{\partial \ln T_i}{\partial \phi} = -\frac{2u_i}{RT_i} \frac{\partial u_i}{\partial z} \tan \phi. \quad (4)$$

Integrating (4) for $\partial \ln T_i / \partial \phi$ at the surface where u_i is defined by (1) then yields

$$T_i(\lambda, \phi, z) = T_i(\phi) = T_{eq} \exp \left(-\frac{c u_{eq}^2}{g} \sin^2 \phi \right), \quad (5)$$

which is a slightly more exact expression than the one given in DCMIP (81). Integrating (4) for $\partial u_i / \partial z$ above the surface, using (5) to evaluate $\partial \ln T_i / \partial \phi$,

$$u_i(\lambda, \phi, z) = u_{eq} \sqrt{1 + 2c z \cos \phi}, \quad (6)$$

which provides a simpler and more accurate expression for the initial wind profile than DCMIP (82). The differences of (5)-(6) from DCMIP (81)-(82) are quite small, but provide a specification for the wind field that is easier to interpret and to apply.

Using (2) and (3), the balanced initial pressure field becomes (with minor approximation):

$$p_i(\lambda, \phi, z) = p_{eq} \exp \left(-\frac{u_{eq}^2}{2R_d T_{eq}} \sin^2 \phi - \frac{gz}{R_d T_{eq}} \right), \quad (7)$$

which corresponds to DCMIP (80). As pointed out in the DCMIP test-case document, for a pressure-based vertical coordinate (7) can be rearranged to provide an equation for the height field (DCMIP eq. 84):

$$z_i(\lambda, \phi, p) = \frac{R_d T_{eq}}{g} \ln \left(\frac{p_{eq}}{p} \right) - \frac{u_{eq}^2 \sin^2 \phi}{2g} \quad (8)$$

Mountain topography

Two different terrain profiles are used for these testcases: one that allows semi-quantitative comparison with the well-documented 2-D SLFLG testcase, and one using the same circular terrain profile as in the DCMIP 2.1 experiment. The circular mountain used in DCMIP 2.1 is specified according to the expression:

$$z_s(\lambda, \phi) = h_0 \exp \left[-\frac{r(\lambda, \phi)^2}{d_0^2} \right] \cos^2 \left[\frac{\pi r(\lambda, \phi)}{\xi_0} \right], \quad (9)$$

(DCMIP, eq. 76), where $r(\lambda, \phi)$ is the great-circle distance from the mountain center at (λ_c, ϕ_c) , as defined in DCMIP (77):

$$r(\lambda, \phi) = \frac{a_{ref}}{X} \arccos[\sin \phi_c \sin \phi + \cos \phi_c \cos \phi \cos(\lambda - \lambda_c)], \quad (10)$$

a_{ref} is the full earth radius, X is the reduced earth-radius scaling factor, $h_0 = 250$ m, $d_0 = 5000$ m, and $\xi_0 = 4000$ m.

The terrain defined in (9) was configured such that the profile along its centerline is identical to the 2-D terrain investigated by SLFLG. Thus, to achieve similarity with the 2-D SLFLG case, we have modified the mountain profile by retaining the 2-D SLFLG terrain shape along the equator, and then extending this terrain along a ridge in the north-south direction, with the height and width gradually reduced to zero approaching the poles (i.e. multiplying the 2-D terrain profile by $\cos \phi$). In this manner, the mountain-wave solution along the equator is very similar to the 2-D solutions published by SLFLG and KSF. For this purpose, we alter the terrain specified in (9)-(10) by defining the distance r used in (9) as the distance along the earth's surface from the ridge axis (at $\lambda = \lambda_c$) in the longitudinal direction. With this modification, the expression for r becomes

$$r(\lambda, \phi) = \frac{a_{ref}}{X} (\lambda - \lambda_c) \cos \phi = r_0(\lambda) \cos \phi, \quad (11)$$

The ridge height z_s is then tapered off toward the poles with a cosine function such that $Nz_s(\lambda_c, \phi)/u_i(\phi)$, a measure of the nonlinearity of the flow, remains independent of ϕ . Similarly, the horizontal length scales of the terrain ($d = d_0 \cos \phi$, $\xi = \xi_0 \cos \phi$) are scaled with latitude so that the ratio of the vertical length scale (u_i/N) to the horizontal scale also does not depend on latitude. The expression for the terrain height then becomes

$$z_s(\lambda, \phi) = h_0 \exp\left[-\frac{r_0(\lambda)^2}{d_0^2}\right] \cos^2\left[\frac{\pi r_0(\lambda)}{\xi_0}\right] \cos(\phi). \quad (12)$$

Model domain configuration for case M1 to compare with the SLFLG 2-D test case

Here, the intent is to define a model configuration that will provide good quantitative agreement with the 2-D test case investigated by SLFLG and KSF. For this purpose we specify a reduce-radius scaling factor of $X = 166.7$, which is one third the scaling factor used for DCMIP 2.1. This larger radius sphere is adopted to minimize the effects of sphere curvature, and to prevent the mountain-wave disturbances from circling the globe during a two-hour simulation. Maintaining similarity with the SLFLG case, we specify the model top $z_{top} = 20$ km, with an absorbing layer employed above $z_h = 10$ km. (The damping in the absorbing layer can be specified using Rayleigh damping as proposed in DCMIP (78)-(79), or another approach, if preferred.) For the ridge terrain profile we find that a horizontal grid spacing of about 1.1° (~ 720 m) and a vertical grid spacing of ~ 500 m is sufficient to accurately capture the wave development of interest above the mountain (to 10 km) and provide good semi-quantitative agreement with the linear analytic solution for the 2-D case. Raising the domain top to 30 km for this case is not advised as curvature effects and other 3-D influences at the higher levels will compromise comparisons with the original 2-D SLFLG test-case. The time step used for the model integration is $\Delta t = 12$ s.

Example MPAS results for case M1: ridge terrain profile

The ridge terrain profile is depicted in Figure 1a. Horizontal cross sections of the perturbation potential temperature θ' and vertical velocity w at 8 km are displayed in Figures 1b and 1c, respectively. The wave structure over the central portion of the ridge is reasonably two-dimensional, with more noticeable three-dimensional structure appearing at higher latitudes, where both the terrain height and wind speed have decreased significantly from their amplitudes along the equator.

To compare results with the 2-D wave structure discussed by SLFLG and KSF, we display in Figure 2a the vertical cross section of the vertical velocity along the ridge centerline (equator) for the terrain profile as defined in (8), but with a maximum height $h_0 = 25$ m to ensure that the wave response is essentially linear. We have also derived the linear analytic solution for the corresponding flow over a 2-D ridge, which is shown in Figure 2b. For reference, we have included the derivation of this linear solution in Appendix A. This wave structure arises due to the combination of shorter scale evanescent waves at low levels forced by the narrow ridges, together with the longer wavelength modes aloft forced by the broader terrain envelope. The good semi-quantitative agreement of the MPAS simulation with the 2-D analytic solution confirms that the grid structure is sufficient to resolve the dominant wave response,

and that the specified ridge profile and the earth-radius reduction allow a reasonable correspondence with the 2-D flat-plane behavior. The trailing perturbations evident at higher levels in Figure 2a, however, reflect the residual 3-D influences due to curvature effects on the reduced radius earth.

Figure 3 displays the vertical cross sections for w along the ridge centerline at 2 h for a maximum terrain height $h_0 = 250$ m, as used by SLFLG and KSF. These fields are quite similar to the 2-D simulations in those papers. Notice that the amplitudes of the waves are slightly stronger than those shown in Figure 2, due to the presence of weak nonlinear effects. These panels illustrate the importance of using consistent numerics in representing the metrics in the terrain-following coordinate transformation. As discussed by KSF, this issue is most critical for the treatment of the coordinate metric ζ_x that appears in the expression for $\omega = u\zeta_x + w\zeta_z$. Figure 3 documents that using either fourth-order (Figure 3a) or second-order (Figure 3b) numerics for the horizontal advection terms yields accurate results provided the coordinate metric ζ_x is computed using the same order numerics. In contrast, using fourth order advection together with second order numerics for the metric term leads to spurious perturbations (Figure 3c), as documented by KSF.

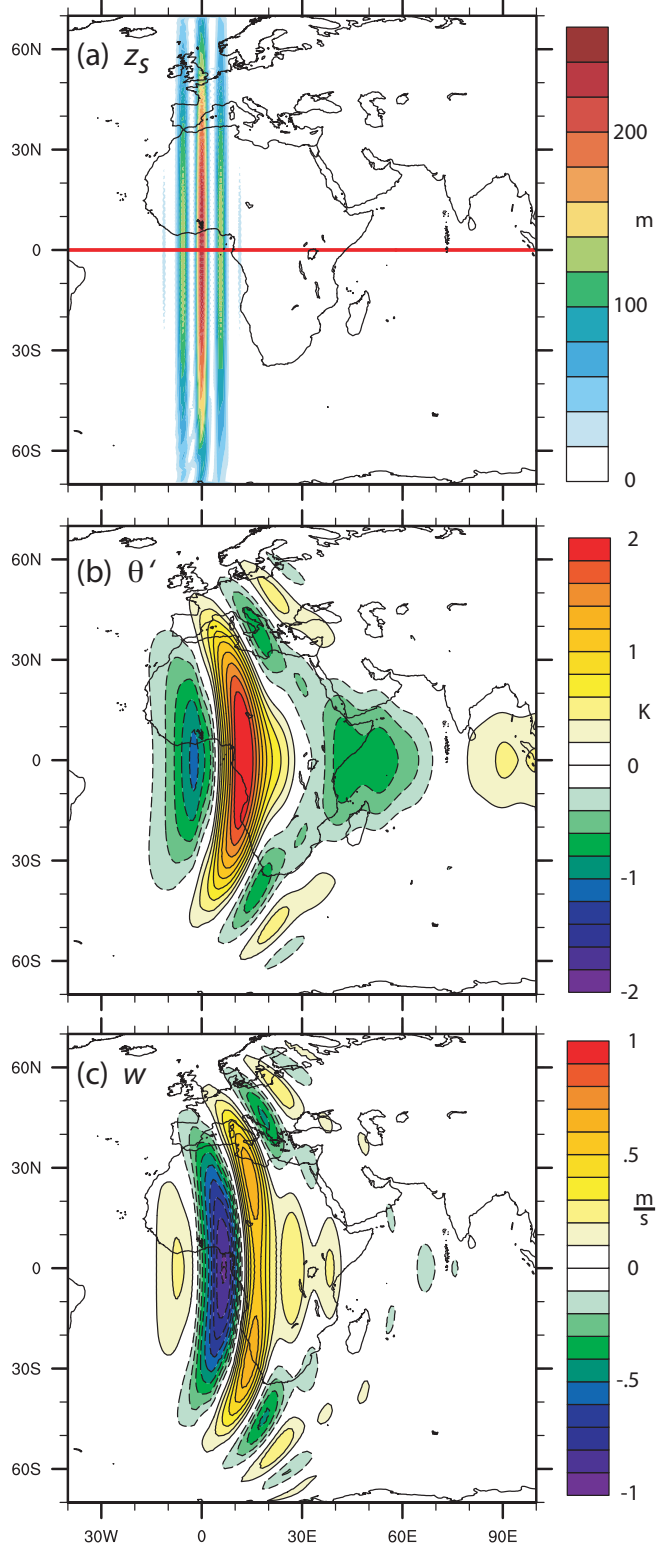


Figure 1. (a) Ridge-like terrain profile z_s as represented in (12). Horizontal cross sections from an MPAS simulation with $h_0 = 250$ m at 8 km at 2 h for (b) Perturbation potential temperature θ' and (c) Vertical velocity w . Geographic boundaries have been left in place for reference.

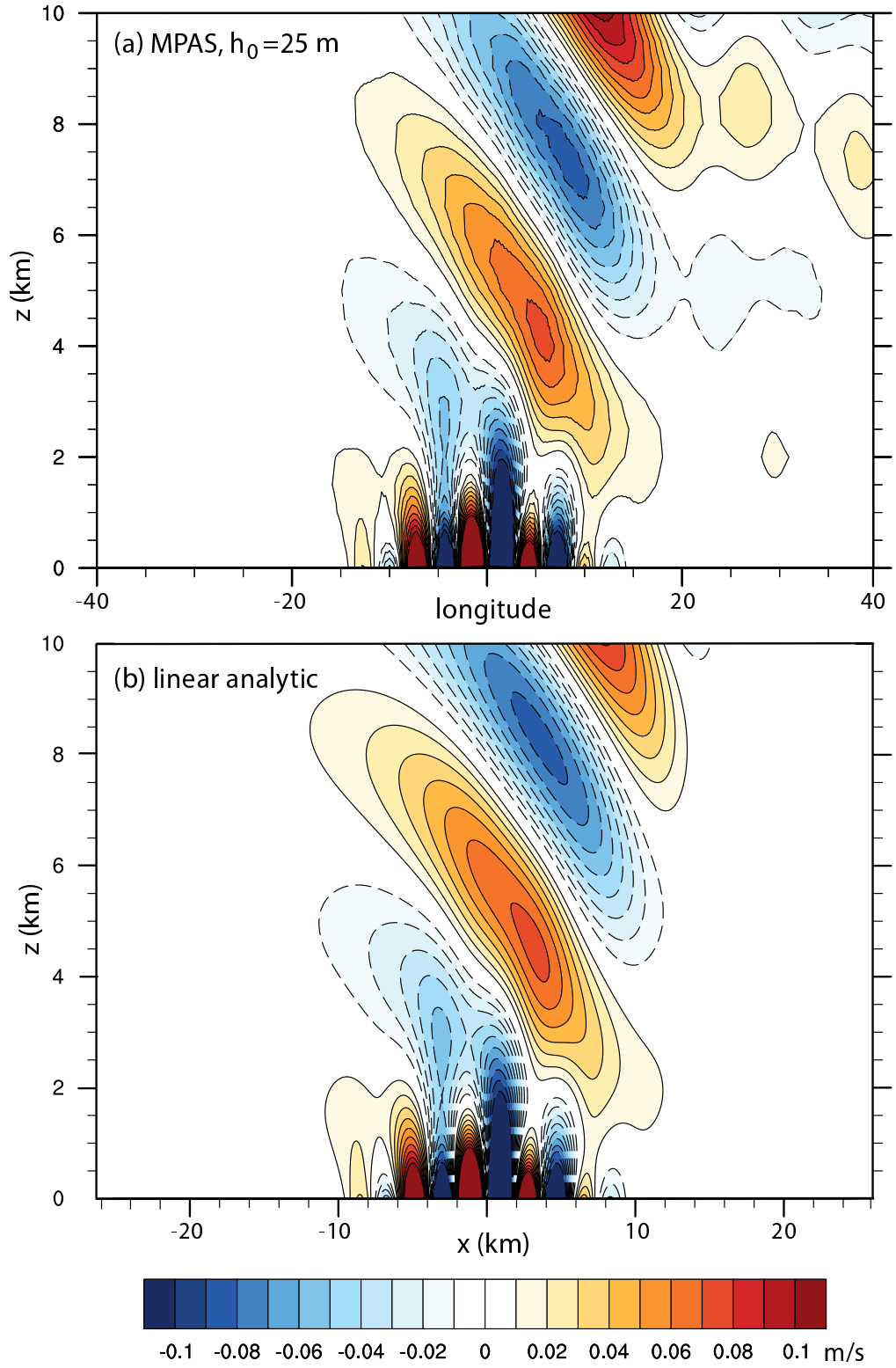


Figure 2. (a) West-east vertical cross section of vertical velocity along the ridge centerline from an MPAS simulation using a linear mountain height $h_0 = 25$ m at 2 h. (b) Vertical cross section of vertical velocity from the 2-D linear analytic solution for $h_0 = 25$ m.

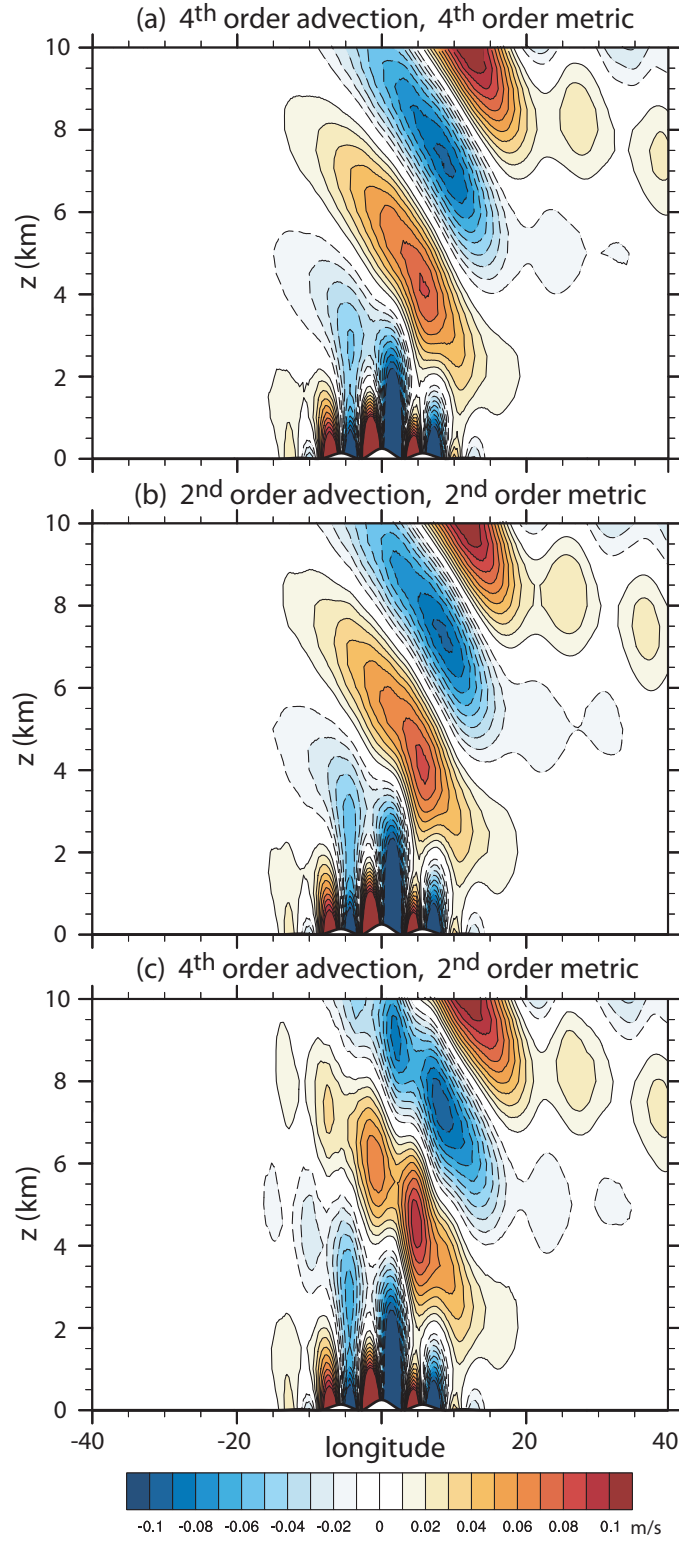


Figure 3. West-east vertical cross sections of vertical velocity along the ridge centerline from MPAS simulations for $h_0 = 250$ m at 2 h. (a) Fourth order horizontal advection with fourth order terrain-following metric terms; (b) second order horizontal advection with second order terrain-following metric terms; and (c) fourth order horizontal advection with second order terrain-following metric terms.

Model domain configuration for case M2 and M3 for a circular mountain

For the circular mountain ((9)), we again specify $X = 166.7$ to reduce curvature effects and prevent disturbances from circling the globe during a two-hour integration. As requested, we have raised the model top to $z_{top} = 30$ km (with a damping layer above 20 km), although this greater domain depth begins to cause significant discrepancies from the corresponding wave structure in a Cartesian geometry due to increasing curvature effects. Because of the more significant smaller scale structure in the nonhydrostatic wave train produced by the circular mountain, we have specified a smaller horizontal grid spacing of ~ 360 m (one-half that used for the ridge mountain simulations). We have specified a nominal vertical grid spacing of 250 m to resolve the smaller scale structure in case M2, and integrate over time using $\Delta t = 6$ s. (A vertical grid spacing of 500 m, as proposed for the original DCMIP 2.1 test case, was found to be less accurate in comparisons with the linear analytic solution for case M2.) For the shear case M3, we initialize the wind field using (6), in which the winds increase from 20 m s^{-1} at the surface to about 80 m s^{-1} at the model top at 30 km. For this case we find that the results are quite similar using either $\Delta z = 250$ m or $\Delta z = 500$ m. The time step is reduced to $\Delta t = 1.5$ s to insure stability with the strong winds aloft.

Example MPAS results for case M2: circular mountain with uniform mean wind

Figure 4 illustrates the evolution of potential temperature and vertical velocity over the circular mountain defined by (9)-(10). The mountain waves developing in response to the uniform flow over this terrain exhibit a strong nonhydrostatic wave train that extends downstream of the mountain as well as laterally. The somewhat noisy behavior at the downstream edge of the expanding wave train appears to be the remnants of the startup vortex arising from the impulsive insertion of the terrain at the beginning of the integration. The potential temperature perturbations extend laterally more rapidly than the vertical velocity and thus are affected sooner by curvature influences. These influences are apparent in the smaller vertical scales appearing in the potential temperature field downstream of the mountain at altitudes between 10-20 km.

Figure 5 provides a more quantitative comparison of the vertical θ and w cross sections at 2 h for the simulation on the reduced-radius sphere with corresponding behavior in a Cartesian geometry. For this purpose, we have also reconfigured the MPAS grid to represent a flat plane of hexagonal grid cells with doubly periodic lateral boundaries. In addition, we have constructed the 3-D linear analytic solution for uniform flow over the circular mountain in a Cartesian geometry (see derivation in Appendix B). In these vertical cross sections, the flat plane simulation exhibits good agreement with the linear analytic solution, confirming that the grid resolution is sufficient to accurately capture the nonhydrostatic wave structure. The small discrepancies in the simulated results are likely due to weak nonlinear effects and slight departures from steady state. In the simulation on the sphere, the vertical velocity field at 2 h is quite similar to the results in a Cartesian geometry. However, as mentioned above, the potential temperature perturbations are exhibiting significant departures at upper levels.

This behavior is further illustrated in horizontal cross sections for these variables. Figure 6 depicts these cross sections at 2 h at a height of 8 km for the simulations on the sphere and flat plane, as well as the linear analytic solution. At this altitude, there is good agreement

Vertical θ and w cross sections along centerline on $X=166.7$ sphere

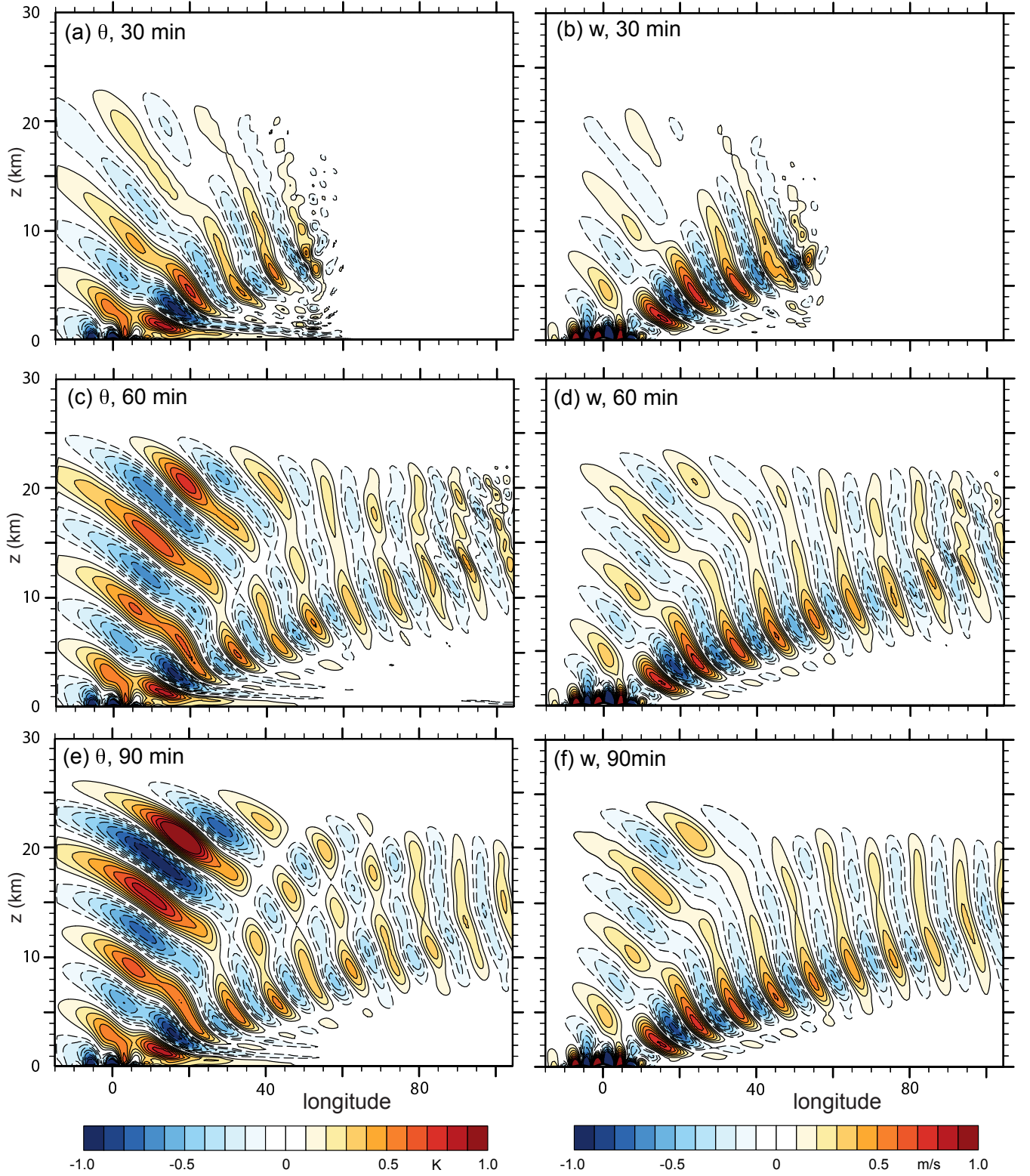


Figure 4. Vertical cross sections for θ' and w in the streamwise direction along the mountain centerline on the reduced radius sphere with $X = 166.7$ at $t = 30, 60,$ and 90 min.

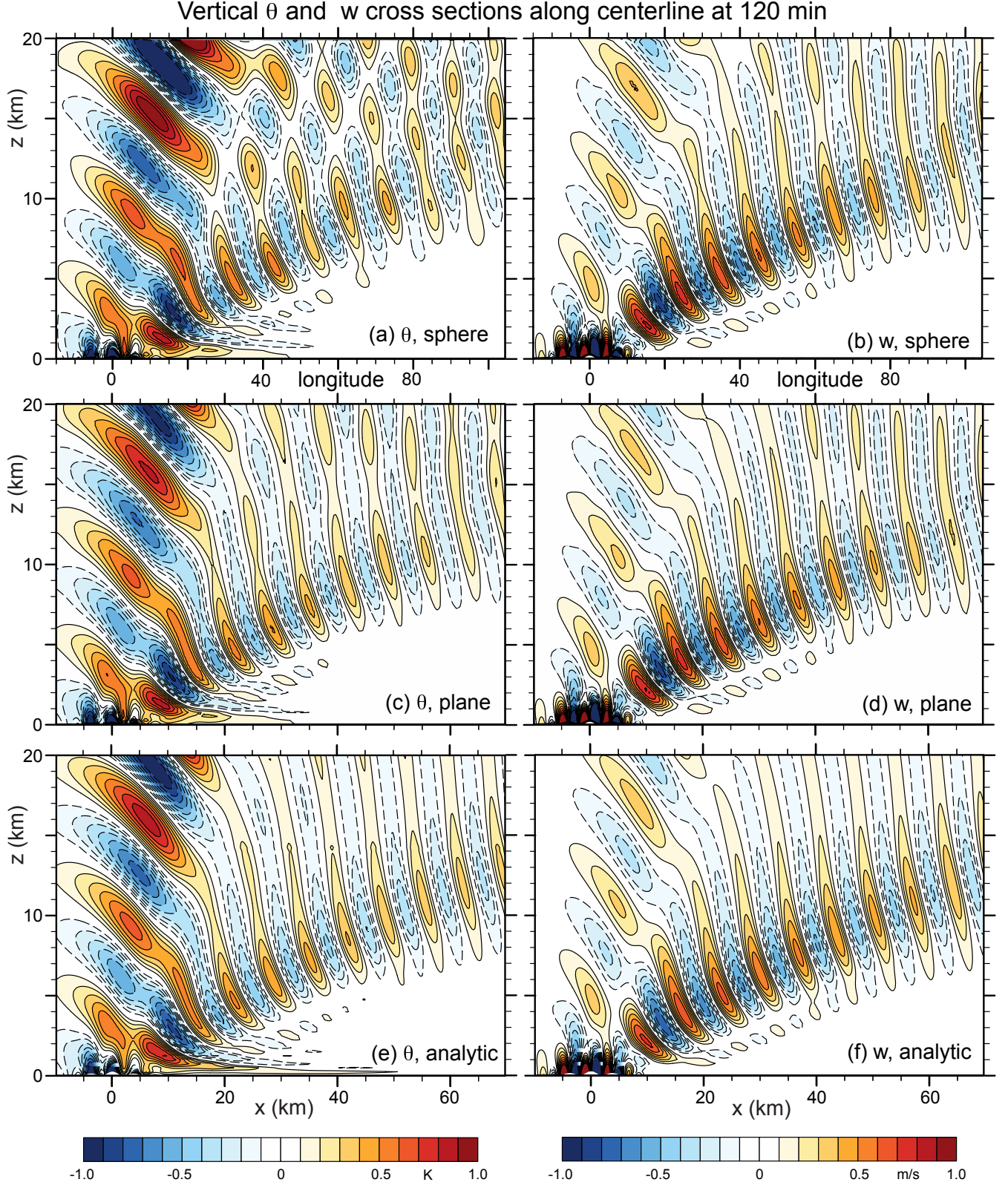


Figure 5. Vertical cross sections for θ' and w in the streamwise direction along the mountain centerline at $t = 120$ min for the (a)-(b) reduced radius sphere and (c)-(d) flat plane. (e)-(f) depicts the corresponding 3-D linear analytic solution from Appendix B.

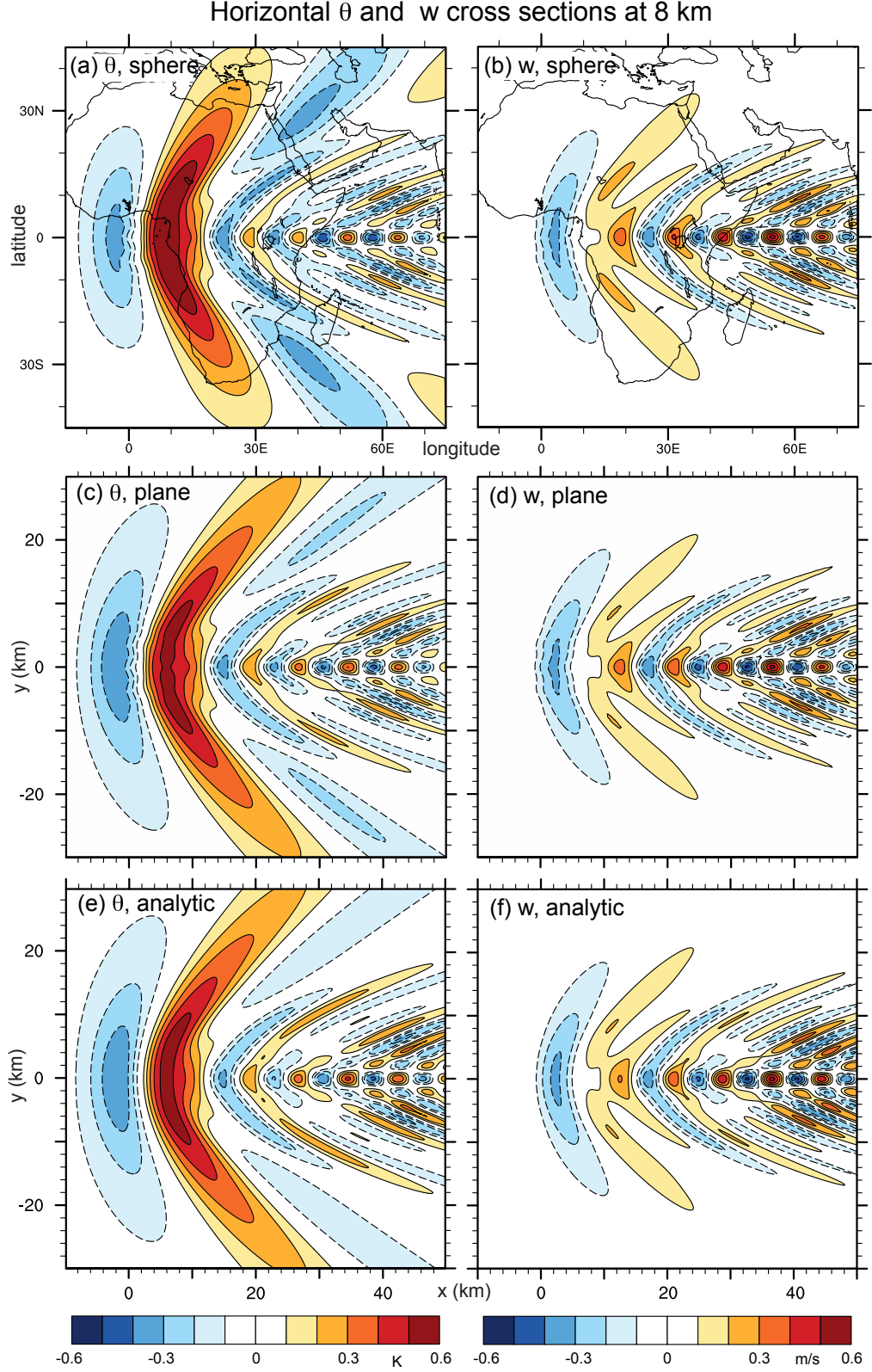


Figure 6. Horizontal cross sections for θ' and w at $z = 8$ km at $t = 120$ min for the (a)-(b) reduced radius sphere and (c)-(d) flat plane. (e)-(f) depicts the corresponding linear analytic solution from Appendix B.

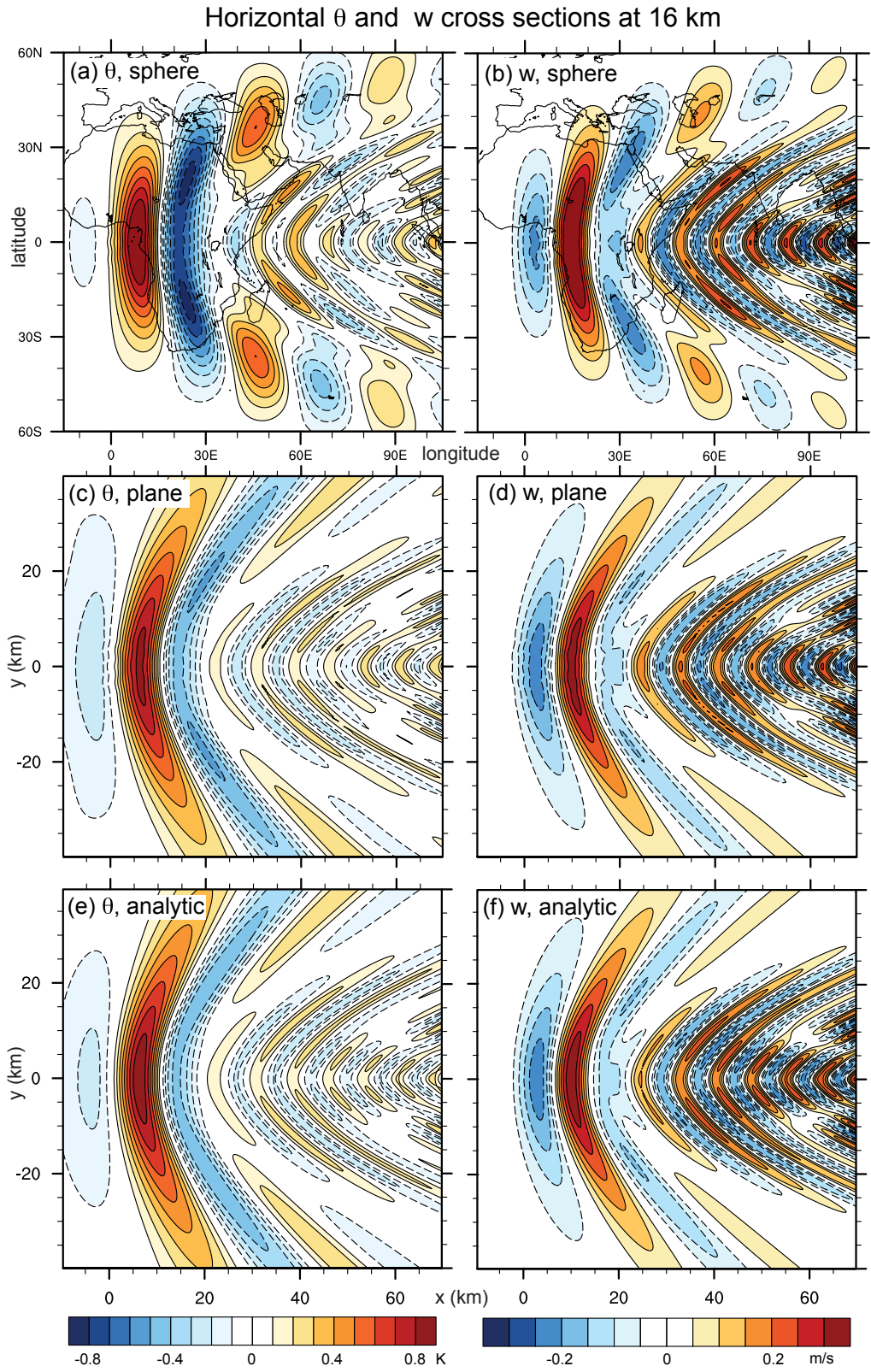


Figure 7. As in Figure 6 except at $z = 16$ km.

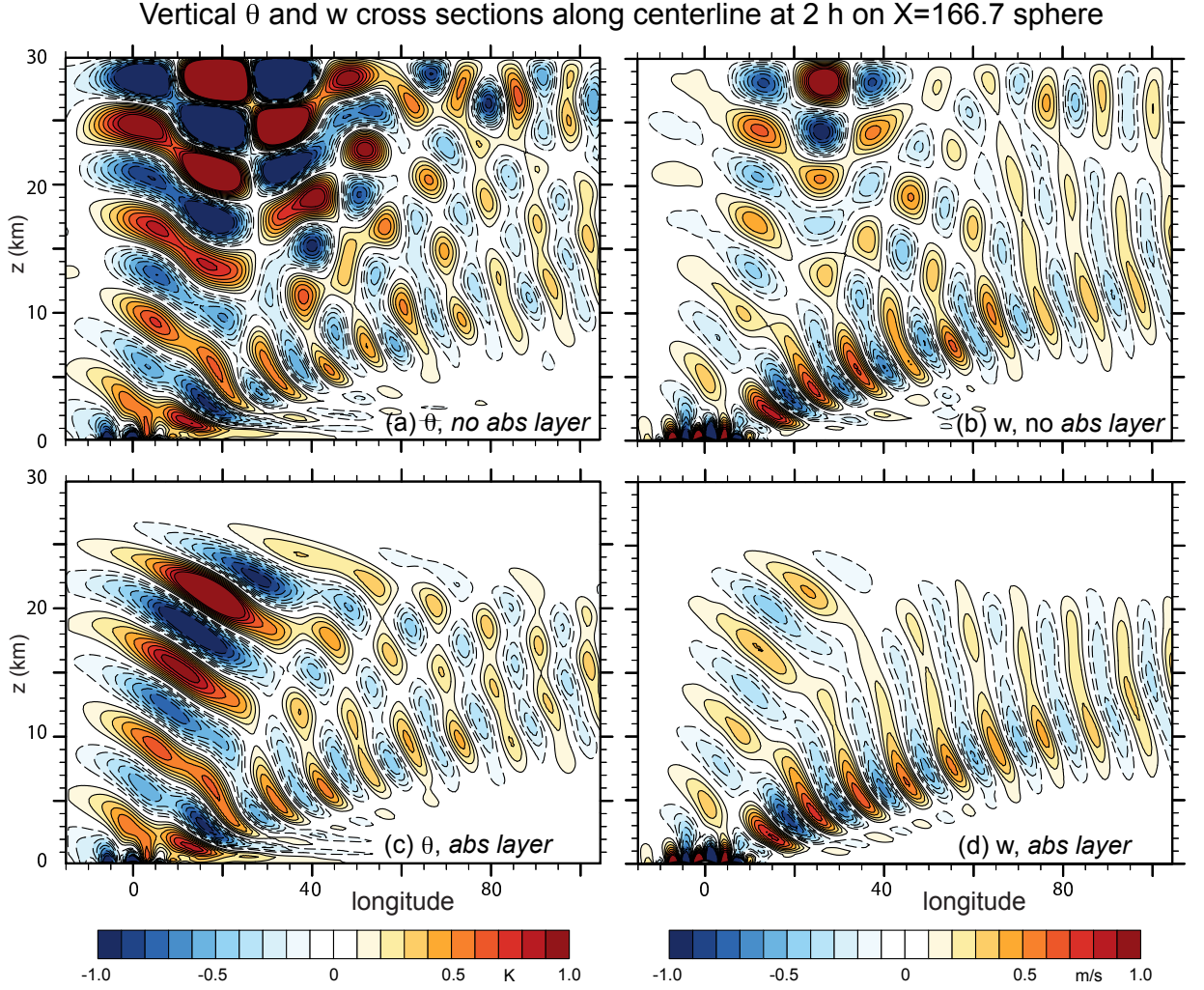


Figure 8. Vertical cross sections for θ' and w in the streamwise direction along the mountain centerline on the reduced radius sphere with $X = 166.7$ at $t = 2$ h (a)-(b) with no upper absorbing layer, and (c)-(d) with an absorbing layer in the region $z = 20\text{--}30$ km.

between the solutions on the sphere and the flat plane. Notice, however, that the potential temperature perturbations extend further in latitude than those for vertical velocity and show some departure from the Cartesian behavior at the higher latitudes. Figure 7 shows these same fields at 2 h at a height of 16 km. At this higher altitude, deviations in the vertical velocity field from that on the flat plane are noticeable, particularly at the higher latitudes. Even greater departures are apparent in the potential temperature perturbations at this height.

To assess the impact of the upper absorbing layer, we reran the simulation for the circular mountain on the $X = 166.7$ reduced-radius sphere (shown in Figures 4-7) with the absorbing layer turned off. The vertical cross sections for the potential temperature and vertical velocity along the equator at 2 h are shown in Figure 8, both with and without the absorbing

layer. These results emphasize the importance of absorbing the upward propagating gravity-wave energy to prevent significant artificial reflection from the upper boundary of the domain.

Example MPAS results for case M3: circular mountain with mean vertical wind shear

Figure 9 displays the time evolution of the vertical cross sections of potential temperature and vertical velocity along the mountain centerline for the wind shear case M3. By 2 h the wave disturbances have propagated to about 270° (180 km) downstream of the mountain. Because of the strong winds aloft shorter wave length components of the mountain waves are trapped below the level where they become evanescent. The energy of these waves is ducted and propagates downstream. Trapped waves with a wave length of about 15 km are particularly evident in the region below 10 km. Figure 10 compares the results at 2 h for simulations with $\Delta z = 500$ m and $\Delta z = 250$ m, respectively. The close agreement of these solutions confirms that for this case, the coarser resolution is sufficient to accurately resolve the mountain wave structure.

The horizontal cross sections for the perturbation potential temperature and vertical velocity at 2 h are displayed in Figure 11 at $z = 8$ km and $z = 16$ km. At the higher levels it appears that curvature effects at high latitudes may be significantly influencing the wave structure, although we have not attempted to quantify these effects.

APPENDIX A

2-D linear analytic solution for a Schär mountain in an isothermal atmosphere

The linear wave equation for flow with an isothermal mean state T_0 and a constant mean wind U is well suited for analysis since it can be written in a form that has constant coefficients. Removing the dependency on the mean density profile

$$w(x, z) = \left(\frac{\rho_0}{\bar{\rho}}\right)^{\frac{1}{2}} w_1(x, z) = \exp\left(\frac{\beta z}{2}\right) w_1(x, z),$$

w_1 is periodic with height and satisfies the wave equation:

$$\nabla^2 w_1 + \left(\frac{N^2}{U^2} - \frac{\beta^2}{4}\right) w_1 = 0, \quad (A1)$$

where

$$N^2 = \frac{g^2}{c_p T_0}, \quad \text{and} \quad \beta = \frac{g}{R_d T_0} \quad (A2)$$

For a single Fourier mode, $w_1(x, z) = \hat{w}_1(k, z) \exp(ikx)$, and (A1) becomes:

$$\frac{d^2 \hat{w}_1}{dz^2} + m^2 \hat{w}_1 = 0 \quad (A3)$$

Vertical θ and w cross sections along centerline on $X=166.7$ sphere

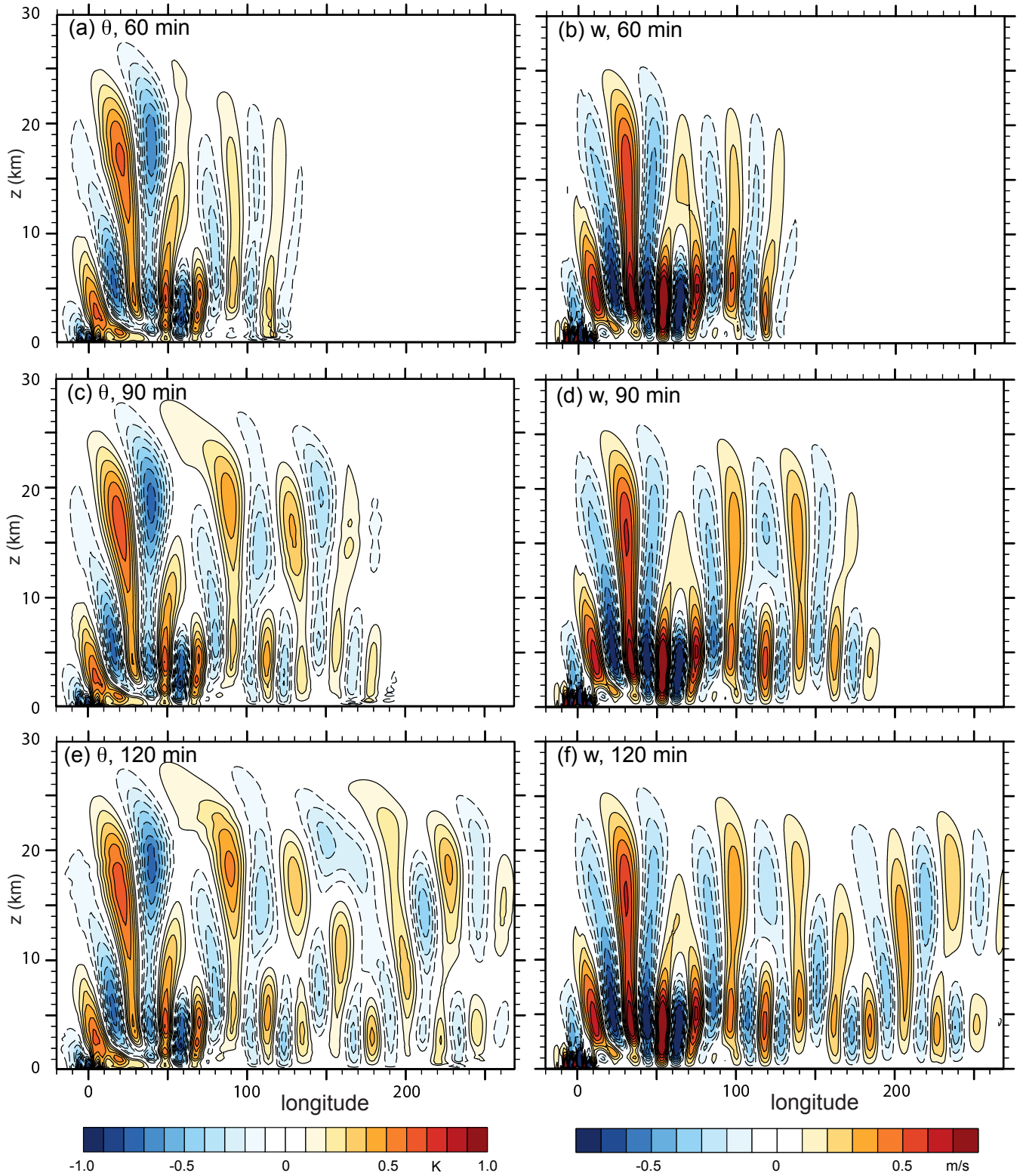


Figure 9. Vertical cross sections for θ' and w in the streamwise direction along the mountain centerline on the reduced radius sphere with $X = 166.7$ for case M3 (vertical shear) at $t = 60, 90,$ and 120 min.

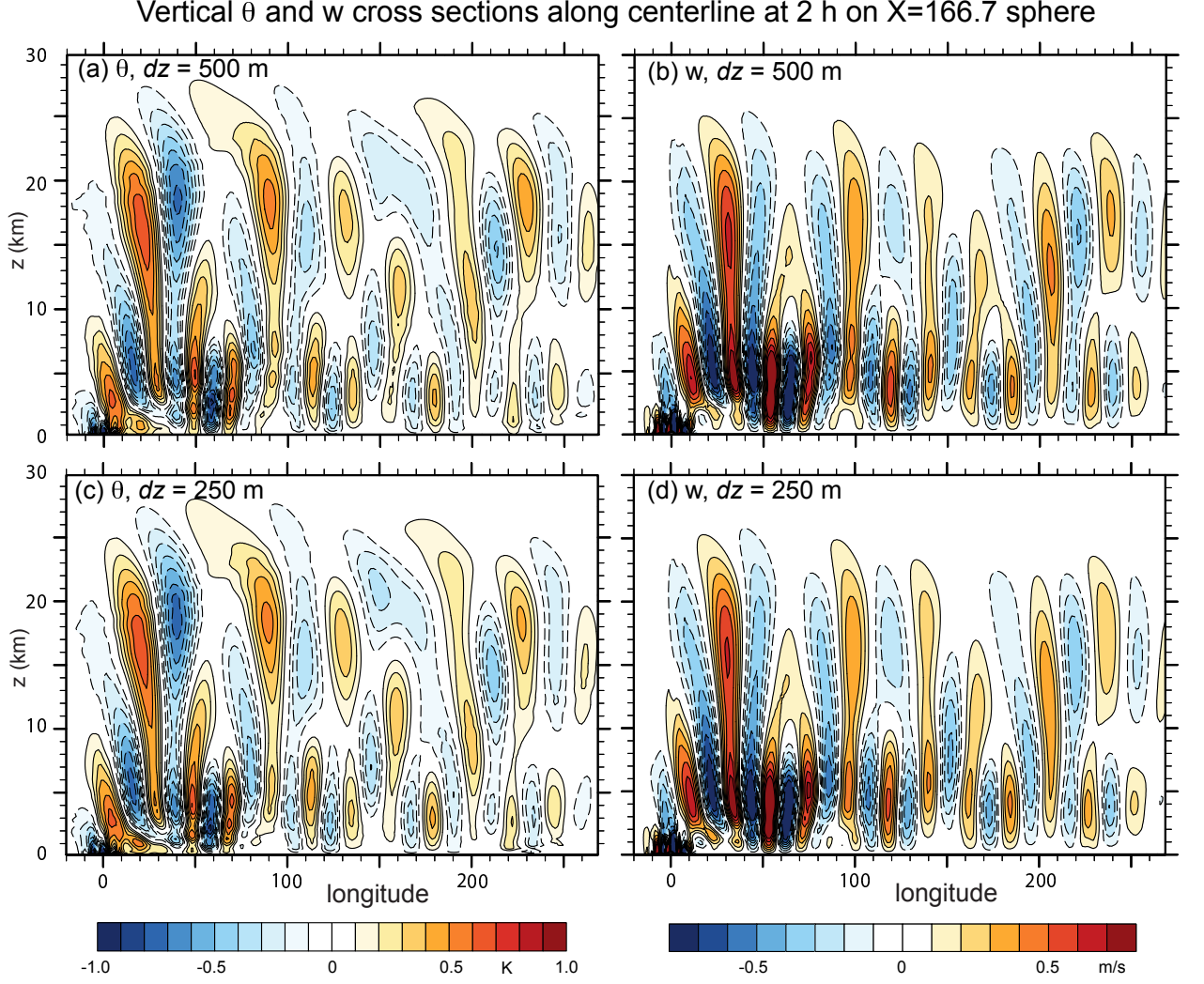


Figure 10. Vertical cross sections for θ' and w in the streamwise direction along the mountain centerline at $t = 120$ min for case M3 (vertical wind shear) for (a)-(b) $dz = 500$ m and (c)-(d) $dz = 250$ m.

where

$$m^2 = \frac{N^2}{U^2} - \frac{\beta^2}{4} - k^2. \quad (A4)$$

The lower boundary terrain profile is given by

$$h(x) = h_0 \exp\left(-\frac{x^2}{d^2}\right) \cos^2 \frac{\pi x}{\xi}, \quad (A5)$$

and its corresponding Fourier transform is

$$\hat{h}(k) = h_0 \int_0^\infty \exp\left(-\frac{x^2}{d^2}\right) [1 + \cos Kx] \cos kx \, dx \quad (A6)$$

$$= \frac{\sqrt{\pi}}{4} h_0 d \left\{ \exp\left[-\frac{d^2}{4}(K+k)^2\right] + 2 \exp\left[-\frac{d^2}{4}k^2\right] + \exp\left[-\frac{d^2}{4}(K-k)^2\right] \right\}, \quad (A7)$$

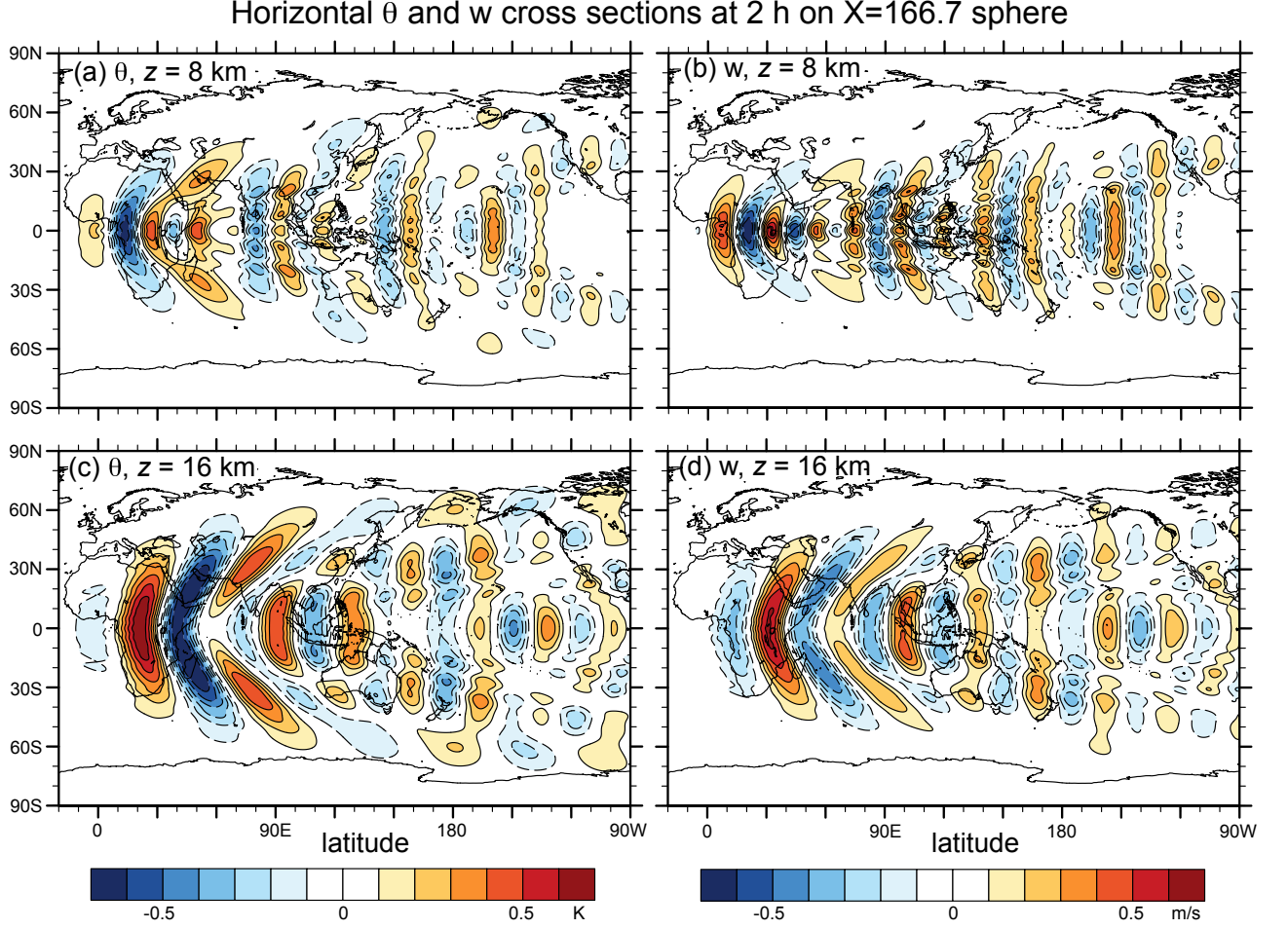


Figure 11. Horizontal cross sections for θ' and w at $t = 120$ min for case M3 on the reduced radius sphere at (a)-(b) $z = 8$ km and (c)-(d) $z = 16$ km.

where $K = 2\pi/\xi$. Solving (A3) subject to the lower boundary condition $\hat{w}_1(k, 0) = ikU\hat{h}(k)$ and applying a radiation condition to ensure upward propagation of wave energy, yields:

$$\hat{w}_1(k, z) = ikU\hat{h}(k) \begin{cases} \exp[i \operatorname{sgn}(k) mz] & \text{for } m^2 > 0 \\ \exp(-|m|z) & \text{for } m^2 < 0 \end{cases}. \quad (\text{A8})$$

Taking the inverse Fourier transform recovers the 2-D vertical velocity field,

$$\begin{aligned} w(x, z) &= \frac{1}{2\pi} \exp\left(\frac{\beta z}{2}\right) \int_{-\infty}^{\infty} \hat{w}_1(k, z) \exp(ikx) dk \\ &= -\frac{U}{\pi} \exp\left(\frac{\beta z}{2}\right) \left\{ \int_0^{k^*} k \hat{h}(k) \sin(mz + kx) dk \right. \\ &\quad \left. + \int_{k^*}^{\infty} k \hat{h}(k) \exp(-|m|z) \sin kx dk \right\} \end{aligned} \quad (\text{A9})$$

where

$$k^* = \left(\frac{N^2}{U^2} - \frac{\beta^2}{4} \right)^{\frac{1}{2}}. \quad (A10)$$

APPENDIX B

3-D linear analytic solution for a circular mountain in an isothermal atmosphere

The 3-D linear wave equation for flow with an isothermal mean state T_0 and a constant mean wind U can be derived in the same manner as the 2-D wave equation in Appendix A. For a single horizontal Fourier mode, $w_1(x, y, z) = \hat{w}_1(k, l, z) \exp[i(kx + ly)]$, the 3-D counterparts to (A3)-(A4) become:

$$\frac{d^2 \hat{w}_1}{dz^2} + m^2 \hat{w}_1 = 0 \quad (B1)$$

with

$$m^2 = \frac{k^2 + l^2}{k^2} \left(\frac{N^2}{U^2} - k^2 \right) - \frac{\beta^2}{4}. \quad (B2)$$

The circular terrain profile is given by

$$h(x) = h_0 \exp\left(-\frac{x^2 + y^2}{d^2}\right) \cos^2\left(\frac{\pi}{\xi} \sqrt{x^2 + y^2}\right), \quad (B3)$$

and its corresponding Fourier transform is

$$\hat{h}(k, l) = 4h_0 \int_0^\infty \int_0^\infty \exp\left(-\frac{x^2 + y^2}{d^2}\right) \cos^2\left(\frac{\pi}{\xi} \sqrt{x^2 + y^2}\right) \cos kx \cos ly \, dy \, dx \quad (B4)$$

Solving (B1) subject to the lower boundary condition $\hat{w}_1(k, l, 0) = ikU\hat{h}(k, l)$ and applying a radiation condition to ensure upward propagation of wave energy, yields:

$$\hat{w}_1(k, l, z) = ikU\hat{h}(k, l) \begin{cases} \exp[i \operatorname{sgn}(k)mz] & \text{for } m^2 > 0 \\ \exp[-|m|z] & \text{for } m^2 < 0 \end{cases}. \quad (B5)$$

The 3-D vertical velocity field is then obtained by taking the inverse Fourier transform of (B5):

$$\begin{aligned} w(x, y, z) &= \frac{1}{4\pi^2} \exp\left(\frac{\beta z}{2}\right) \int_{-\infty}^\infty \int_{-\infty}^\infty \hat{w}_1(k, l, z) \exp[i(kx + ly)] \, dk \, dl \\ &= -\frac{U}{\pi^2} \exp\left(\frac{\beta z}{2}\right) \int_0^\infty \left\{ \int_0^{k^*} k \hat{h}(k, l) \sin(mz + kx) \, dk \right. \\ &\quad \left. + \int_{k^*}^\infty k \hat{h}(k, l) \exp[-|m|z] \sin kx \, dk \right\} \cos ly \, dl, \end{aligned} \quad (B6)$$

where k^* is the value of k for which $m = 0$ in (B2). To evaluate this linear solution, the forward transform of the terrain (B4) and the inverse transform to recover w in (B6) are integrated numerically.

References

- Klemp, J. B., W. Skamarock, and O. Fuhrer, 2003: Numerical consistency of metric terms in terrain-following coordinates. *Mon. Wea. Rev.*, **131**, 1229–1239.
- Schär, C., D. Leuenberger, O. Fuhrer, D. Lüthi, and C. Girard, 2002: A new terrain-following vertical coordinate formulation for atmospheric prediction models, *Mon. Wea. Rev.*, **130**, 2459–2480.
- Skamarock, W. C., J. B. Klemp, M. G. Duda, L. Fowler, S.-H. Park, and T. D. Ringler, 2012: A Multi-scale Nonhydrostatic Atmospheric Model Using Centroidal Voronoi Tessellations and C-Grid Staggering. *Mon. Wea. Rev.*, **240**, 3090–3105.
- Ullrich, P. A., C. Jablonowski, J. Kent, P. H. Lauritzen, R. D. Nair, and M. A. Taylor, 2012: Dynamical Core Model Intercomparison Project (DCMIP) Test Case Document. Available at https://www.earthsystemcog.org/site_media/docs/DCMIP-TestCaseDocument_v1.7.pdf